The Astrophysical Journal Supplement Series, 197:13 (11pp), 2011 November doi:10.1088/0067-0049/197/1/13

KEPLER-15b: A HOT JUPITER ENRICHED IN HEAVY ELEMENTS AND THE FIRST *KEPLER* MISSION PLANET CONFIRMED WITH THE HOBBY–EBERLY TELESCOPE*

Michael Endl[1], Phillip J. MacQueen[1], William D. Cochran[1], Erik J. Brugamyer[2], Lars A. Buchhave[3], Jason Rowe[4], Phillip Lucas[5], Howard Isaacson[6], Steve Bryson[7], Steve B. Howell[7], Jonathan J. Fortney[8], Terese Hansen[9], William J. Borucki[7], Douglas Caldwell[7], Jessie L. Christiansen[7], David R. Ciardi[10], Brice-Olivier Demory[11], Mark Everett[12], Eric B. Ford[13], Michael R. Haas[7], Matthew J. Holman[14], Elliott Horch[15], Jon M. Jenkins[16], David J. Koch[7], Jack J. Lissauer[7], Pavel Machalek[17], Martin Still[7], William F. Welsh[18], Dwight T. Sanderfer[16], Shawn E. Seader[16], Jeffrey C. Smith[16], Susan E. Thompson[16], and Joseph D. Twicken[16]

[1] McDonald Observatory, The University of Texas at Austin, Austin, TX 78712, USA
[2] Astronomy Department, The University of Texas at Austin, Austin, TX 78712, USA
[3] Niels Bohr Institute, University of Copenhagen, Denmark Centre for Star and Planet Formation, University of Copenhagen, Denmark
[4] SETI Institute, Moffett Field, CA 94035, USA
[5] Centre for Astrophysics Research, University of Hertfordshire, College Lane, Hatfield AL10 9AB, UK
[6] Department of Astronomy, University of California, Berkeley, CA 94720, USA
[7] NASA-Ames Research Center, Moffett Field, CA 94035, USA
[8] Department of Astronomy and Astrophysics, University of California, Santa Cruz, CA 95064, USA
[9] Niels Bohr Institute, University of Copenhagen, Denmark
[10] NASA Exoplanet Science Institute/Caltech, Pasadena, CA 91125, USA
[11] Department of Earth, Atmospheric and Planetary Sciences, Massachusetts Institute of Technology, Cambridge, MA 02139, USA
[12] NOAO, 950 N. Cherry Ave., Tucson, AZ 85719, USA
[13] Astronomy Department, University of Florida, 211 Bryant Space Sciences Center, Gainesville, FL 32111, USA
[14] Harvard-Smithsonian Center for Astrophysics, 60 Garden Street, Cambridge, MA 02138, USA
[15] Department of Physics, Southern Connecticut State University, New Haven, CT 06515, USA
[16] SETI Institute/NASA-Ames Research Center, Moffett Field, CA 94035, USA
[17] SETI Institute, 189 North Bernardo Ave 100, Mountain View, CA 94043, USA
[18] Astronomy Department, San Diego State University, San Diego, CA 92182, USA
Received 2011 July 8; accepted 2011 October 18; published 2011 November 4

ABSTRACT

We report the discovery of Kepler-15b (KOI-128), a new transiting exoplanet detected by NASA's *Kepler* mission. The transit signal with a period of 4.94 days was detected in the quarter 1 (Q1) *Kepler* photometry. For the first time, we have used the High Resolution Spectrograph (HRS) at the Hobby–Eberly Telescope (HET) to determine the mass of a *Kepler* planet via precise radial velocity (RV) measurements. The 24 HET/HRS RVs and 6 additional measurements from the Fibre-fed Échelle Spectrograph spectrograph at the Nordic Optical Telescope reveal a Doppler signal with the same period and phase as the transit ephemeris. We used one HET/HRS spectrum of Kepler-15 taken without the iodine cell to determine accurate stellar parameters. The host star is a metal-rich ([Fe/H] $= 0.36 \pm 0.07$) G-type main-sequence star with $T_{\rm eff} = 5515 \pm 124$ K. The semi-amplitude K of the RV orbit is $78.7^{+8.5}_{-9.5}$ m s^{-1}, which yields a planet mass of $0.66 \pm 0.1\ M_{\rm Jup}$. The planet has a radius of $0.96 \pm 0.06\ R_{\rm Jup}$ and a mean bulk density of 0.9 ± 0.2 g cm^{-3}. The radius of Kepler-15b is smaller than the majority of transiting planets with similar mass and irradiation level. This suggests that the planet is more enriched in heavy elements than most other transiting giant planets. For Kepler-15b we estimate a heavy element mass of 30–40 $M_\oplus$.

Key words: planetary systems – stars: individual (Kepler-15, KOI-128, KIC 11359879, 2MASS J19444814+4908244) – techniques: image processing – techniques: photometric – techniques: radial velocities – techniques: spectroscopic

Online-only material: color figures

1. INTRODUCTION

The *Kepler* mission is designed to provide the very first estimate of the frequency of Earth-size planets in the habitable zone of Sun-like stars. The *Kepler* spacecraft continuously monitors 156,453 stars (Borucki et al. 2011) to search for the signatures of transiting planetary companions. The mission is described in detail in Borucki et al. (2010).

The small transit depth of 84 ppm produced by an Earth-size planet defined the photometric precision requirement of *Kepler* at 20 ppm over 6.5 hr for a 12th magnitude Sun-like star. *Kepler* is achieving a precision of 30 ppm or better over a large dynamic range (Jenkins et al. 2010b). The constant stream of photometry at this precision level makes the detection of transits of giant planets, with transit depths of ≈10,000 ppm, relatively easy. Furthermore, giant planets also produce larger radial velocity (RV) amplitudes that allow the planet to be confirmed in short time. It is thus no surprise that the majority of early Kepler planets were gas giant planets in short periodic orbits: Kepler-5b, 6b, 7b, and 8b (Koch et al. 2010; Dunham et al. 2010; Latham et al. 2010; Jenkins et al. 2010a). As all *Kepler* light curves from the first four months are publicly available, hot Jupiters are also confirmed by other groups, e.g., KOI-428b (Santerne et al. 2011). However, Jupiter-class planets

* Based on observations obtained with the Hobby–Eberly Telescope, which is a joint project of the University of Texas at Austin, the Pennsylvania State University, Stanford University, Ludwig-Maximilians-Universität München, and Georg-August-Universität Göttingen.

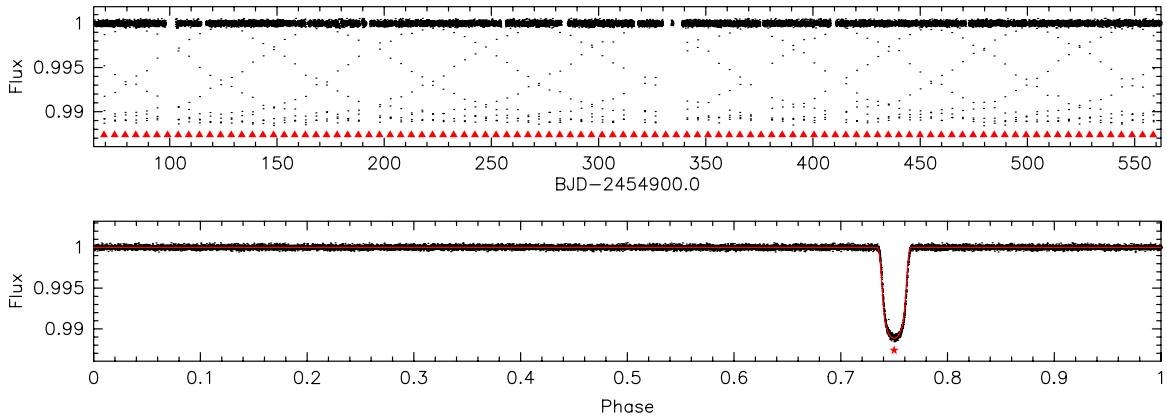

Figure 1. *Kepler* light curve of Kepler-15. The top panel displays the detrended (using a median filter) Q1 to Q6 time series photometry. The triangles mark the times of the transits. The lower panel contains the data phased to the transit period of 4.943 days, with the transit at phase 0.75.

(A color version of this figure is available in the online journal.)

represent the minority of *Kepler* planet candidates, Borucki et al. (2011) derive an intrinsic frequency of Jupiter-size planets ($0.55\ R_{\rm Jup} < R_{\rm p} < 1.36\ R_{\rm Jup}$) of only 2%.

In this paper we describe Kepler-15b, the first giant planet from the *Kepler* mission confirmed with the Hobby–Eberly Telescope (HET) at McDonald Observatory. We use the HET to observe KOIs with a period and mass range (typically in the giant planet range) that make them suitable for queue scheduled observations. In 2010 we spent a total of 65 hr of HET time on the *Kepler* field and collected data for 11 KOIs. Besides the planet presented here, we have confirmed several other giant planets around *Kepler* stars, e.g., Kepler-17b (Désert et al. 2011). The remaining HET planet confirmations will be included in a catalog of *Kepler* giant planets (D. Caldwell et al. 2012, in preparation).

Additional RV measurements for Kepler-15 were also collected with the FIbre-fed Échelle Spectrograph (FIES) at the 2.5 m Nordic Optical Telescope (NOT) that are fully consistent with the HET/High Resolution Spectrograph (HRS) results. In the following sections, we describe the *Kepler* photometry for Kepler-15 and the subsequent ground-based follow-up observations to reject a false-positive and to confirm the planet. Finally, we will discuss the radius of Kepler-15b and the planet's internal composition.

2. *KEPLER* PHOTOMETRY AND TRANSIT SIGNATURE

2.1. Light Curve Analysis

Kepler-15 was already identified as a planet candidate in the 35 days of the first quarter (Q1) of *Kepler* photometry and was assigned the Kepler-Object-of-Interest (KOI) identifier KOI-128. The target star has a Kepler magnitude ($K_{\rm p}$) of 13.76 ($K_{\rm p}$ is defined by the *Kepler* response function and covers the wavelength range of 4230–8970 Å; Koch et al. 2010). Kepler-15 is 2MASS J19444814+4908244 and its basic parameters are summarized in Table 1. Processing of the photometry was carried out using the standard *Kepler* pipeline (Jenkins et al. 2010b). The data were sampled at the typical 30 minute "long cadence." Figure 1 displays the *Kepler* light curve for Kepler-15. The top panel shows the Photometric Analysis (PA) light curve for Q1 through Q6 after removal of data artifacts using a 2 day median filter (in-transit photometry was masked prior to the application of this filter). The detrended out-of-transit data have a standard deviation of 223 ppm. The lower panel shows the data phased to the candidate period of 4.943 days. A more detailed view of the phased transit light curve is given in Figure 2. The transit has a duration of 3.5 hr

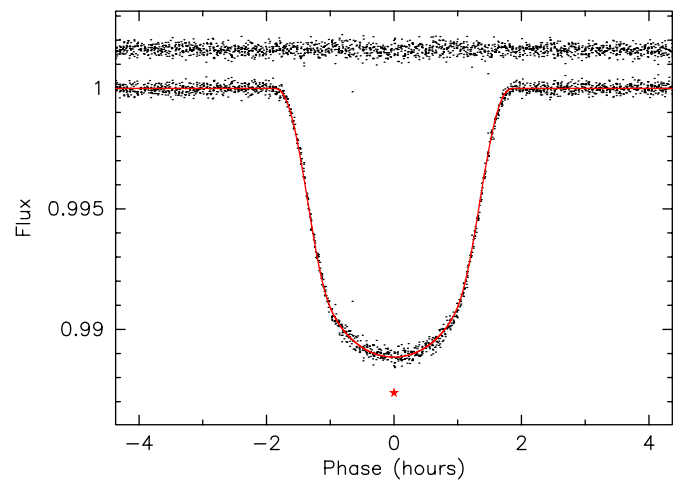

Figure 2. Phased Kepler-15 transit light curve. The dots represent the *Kepler* photometric data while the solid line displays the best-fit transit model. The transit has a photometric depth of 11,127 ± 14 ppm and lasts 3.5 hr. The residuals after subtracting the transit model are shown offset above the light curve.

(A color version of this figure is available in the online journal.)

Table 1
Basic Parameters of the Target Star Kepler-15

Parameter	Value	Source
Kepler No.	15	
Kepler-Object-of-Interest (KOI) No.	128	
Kepler Input Catalog (KIC) No.	11359879	
2MASS	J19444814+4908244	2MASS[a]
R.A. (2000)	19:44:48.16	2MASS
Decl. (2000)	49:08:24.44	2MASS
$K_{\rm p}$ (mag)	13.76	KIC[b]
g (mag)	14.27	KIC
J (mag)	12.58	2MASS
H (mag)	12.28	2MASS
K (mag)	12.22	2MASS

Notes.
[a] Cutri et al. (2003).
[b] Brown et al. (2011).

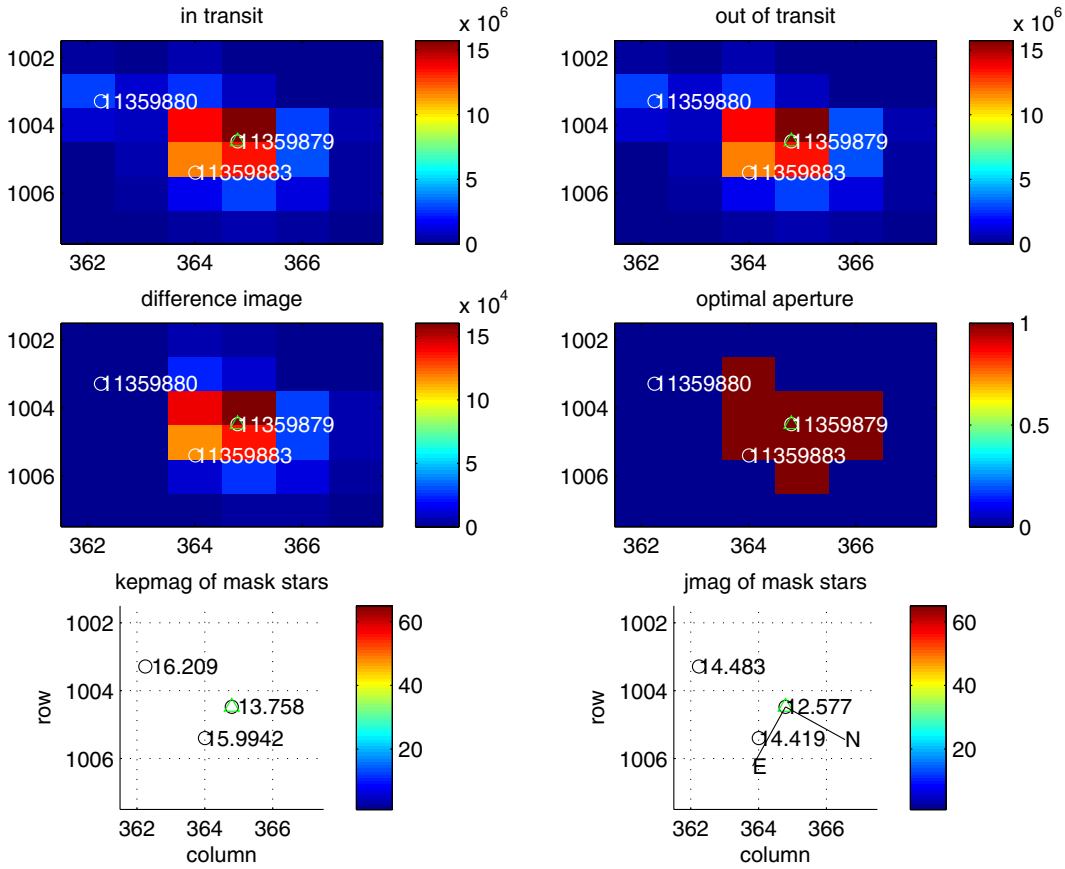

Figure 3. Difference images for Kepler-15 (KIC 11359879). Each panel shows the same section of the CCD (*x*-axis is the pixel column and *y*-axis is the pixel row). One *Kepler* pixel is 3.96 arcsec^2. The color coding represents the flux level in each pixel. The top two panels display the in and out of transit images and the difference image is shown in the middle left panel. The color maps used in these figures are normalized to the range of values in each image (this allows an easy comparison of these images). The optimal aperture for the photometry can be seen for comparison in the middle right panel. The lower two panels show the field, its orientation on the chip, and the K_p- and J-band magnitudes of nearby KIC stars.

(A color version of this figure is available in the online journal.)

and a photometric depth of 11,127 ± 14 ppm. The period of the transit is 4.9427813 ± 0.000002 days. We have also searched for a secondary eclipse and transit timing variations (TTVs) in the Kepler-15 light curve, but so far have found no significant variability indicating the detection of these effects. The Kepler-15 photometry is available at the Multi-Mission Archive (MAST[19]) at the Space Telescope Science Institute.

2.2. Difference Image Analysis

To eliminate the possibility that the transit signatures are due to transits on a background star, the change in centroid location during transit was examined using the difference image method described in Torres et al. (2011). This method fits the measured *Kepler* pixel response function (PRF; Bryson et al. 2010) to a difference image formed from the average in-transit and average out-of-transit pixel images. This difference image method has the advantage of directly measuring the location of the transiting signal. In addition, the PRF is fit to the out-of-transit image to measure the position of the target star. An example of the average images including the optimal aperture pixels used to create the light curve and the local stellar scene is shown in Figure 3.

The out-of-transit centroid is subtracted from the difference image centroid to provide the offset of the transit signal location from the target star. The offsets from Q1 through Q7 are shown as the green crosses in the left panel of Figure 4, where the arms of the green crosses show the uncertainty in R.A. and Decl. We see that in all quarters the transit signal location is consistently offset to the west by 0.″1 ± 0.″019. The robust average across quarters, weighted by the quarterly uncertainty, is shown by the magenta cross, with the solid circle giving its 3σ uncertainty radius. This average centroid observation is offset by about 0.″1 with a significance of 5.7σ. The right panel of Figure 4 shows the transit signal source estimated by correlating the light curve from the modeled transit with observed photocenter motion (Jenkins et al. 2010a). Photocenter motion also shows a statistically significant (17σ) transit signal location offset, but the offsets from the two methods are in significant disagreement, suggesting that these offsets are due to measurement bias.

The uncertainty in PRF-fit centroids is based on the propagation of pixel-level uncertainty and does not include a possible PRF fit bias. Sources of PRF fit bias include scene crowding, because the fit is of a single PRF assuming a single star, as well as PRF error. The measured offset is the difference between the centroids of the difference and out-of-transit images, so common biases such as PRF error should cancel. Bias due to crowding, however, will not cancel because, to the extent that variations in other field stars are not correlated with transits, field stars will not contribute to the difference image. In other words, the difference image will have the appearance of a single star where the transit occurs, so there is no crowding bias in the difference image PRF fit.

[19] http://archive.stsci.edu/kepler/data_search/search.php

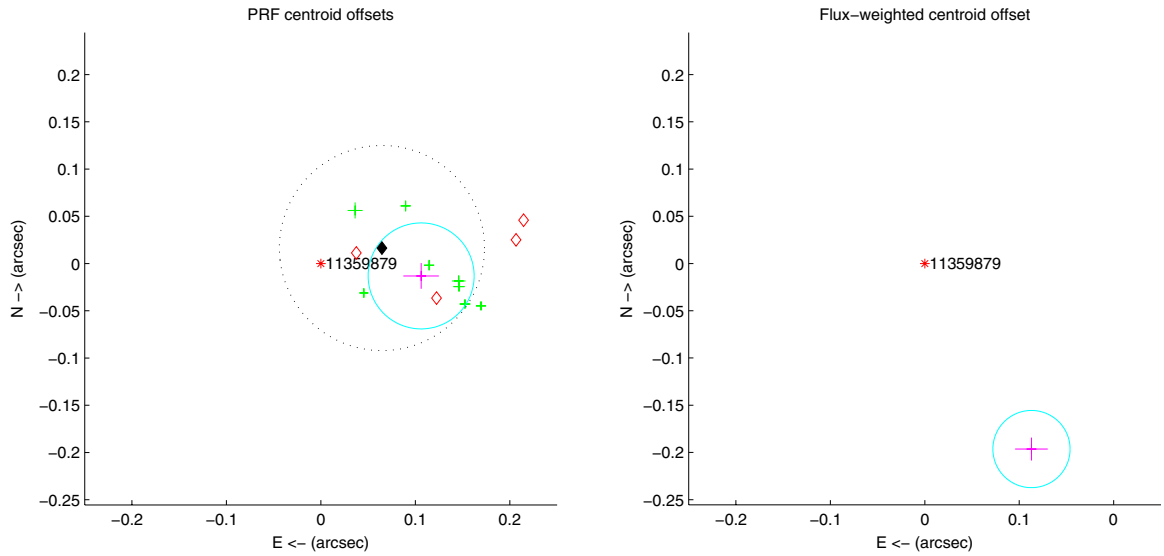

Figure 4. Pixel Response Function (PRF) centroid offset (left panel) and flux-weighted centroid offset (right panel) for Kepler-15 (KIC 11359879). The observed centroid is displayed as a large cross with a solid circle showing the 3σ uncertainty. The left panel also contains the individually observed point-spread function centroids for Q1 through Q7 (small crosses) as well as the centroid results from our test (see the text for details) to estimate the effect of crowding (small diamonds). A systematic offset to the west of 0.″1 due to crowding is observed and reproduced by the test results.

(A color version of this figure is available in the online journal.)

To investigate the possibility that the observed offsets are due to PRF-fit bias caused by crowding we modeled the local scene using stars from the Kepler Input Catalog supplemented by UKIRT observations (see Section 3.2) and the measured PRF, induced the transit on Kepler-15 in the model, and performed the above PRF fit analysis on the model difference and out-of-transit images. The resulting model offsets for quarters one through four is shown in Figure 4 as open diamonds. (Only four quarters are shown because the model is very nearly periodic with a period of one year.) The robust average of the model offsets, again weighted by propagated uncertainty, is shown as the filled diamond, with the dotted circle showing the average model 3σ uncertainty. We see that the model points are consistently offset to the west, and the observed average is well contained within the model 3σ uncertainty. This is consistent with the observed in-transit centroid offsets being due to PRF fit bias (mostly) due to crowding. (A more detailed and general description of the analysis of PRF fit bias will be presented in a forthcoming paper: S. Bryson et al. 2011, in preparation.) The difference image completely rules out that the transits occur on the second star in the aperture (KIC 11359883). A transit on KIC 11359883 would appear in the difference image as a star centered on the pixel containing KIC 11359883. We therefore can be highly confident that the transit signal is due to transits on Kepler-15.

3. CONFIRMATION BY GROUND-BASED FOLLOW-UP OBSERVATIONS

3.1. Reconnaissance Spectroscopy

As part of the *Kepler* Follow-up Observing Program (FOP) strategy (Gautier et al. 2010), we first obtained two reconnaissance spectra of Kepler-15 with the Tull Coudé Spectrograph (Tull et al. 1995) at the Harlan J. Smith 2.7 m Telescope at McDonald Observatory. The two spectra were obtained on 2009 August 8th and September 3rd (UT), respectively. The first spectrum was observed with a spectral resolving power of $R = 40{,}000$ and an exposure time of 1200 s that yield a signal-to-noise ratio (S/N) of 26 at 5220 Å. The second reconnaissance spectrum was taken at $R = 60{,}000$ with an exposure time of 1800 s and an S/N of 22 (at 5220 Å).

We then compared the reconnaissance spectra with a library of stellar templates by cross-correlating them with a single Echelle order ranging from 5180 to 5260 Å. The step size between individual templates are 250 K for $T_{\rm eff}$, 0.5 dex for log g, and 1 km s^{-1} for $v \sin i$. [Fe/H] is fixed to solar metallicity. The template with the highest normalized cross-correlation peak function is selected as the best match. This comparison resulted in the following stellar parameters: $T_{\rm eff} = 5500$ K, log $g = 4.0$ (first spectrum), log $g = 4.5$ (second spectrum), and $v \sin i = 2$ km s^{-1}. The absolute RV of Kepler-15 is -20 km s^{-1} and the two measurements differ by less than 1 km s^{-1} (which is within the measurement uncertainty) between the two visits (which were separated by one month). These results exclude the scenario where a grazing eclipsing binary produces a false-alarm (a binary should have produced a significant RV shift between the two reconnaissance spectra). Despite the low S/N we also examined the Ca II H & K lines to check for any strong chromospheric emission that would indicate an active star. We did not detect any sign of emission in either spectra. From this initial reconnaissance of Kepler-15 we concluded that this target is suitable for Doppler follow-up observations.

3.2. Imaging

A seeing limited image of the field around Kepler-15 was obtained at Lick Observatory's 1 m Nickel telescope using the Direct Imaging Camera. A single one-minute exposure was taken in the I band (7500–10500 Å), resulting in an image with seeing of approximately 1.″5. Observations occurred under clear skies and new moon during an observing run in 2010 July 8–10. The I-band image is shown in Figure 5. With the exception of the nearby star KIC 11359883 ($K_{\rm p} = 15.99$), no other object is detected inside the optimal aperture of Kepler-15.

A deep J-band image of the field was obtained at UKIRT (see Figure 6). Three additional objects that are located within the optimal aperture are detected in the UKIRT image. Object 1 is a star close to KIC 11359883 and estimated to have

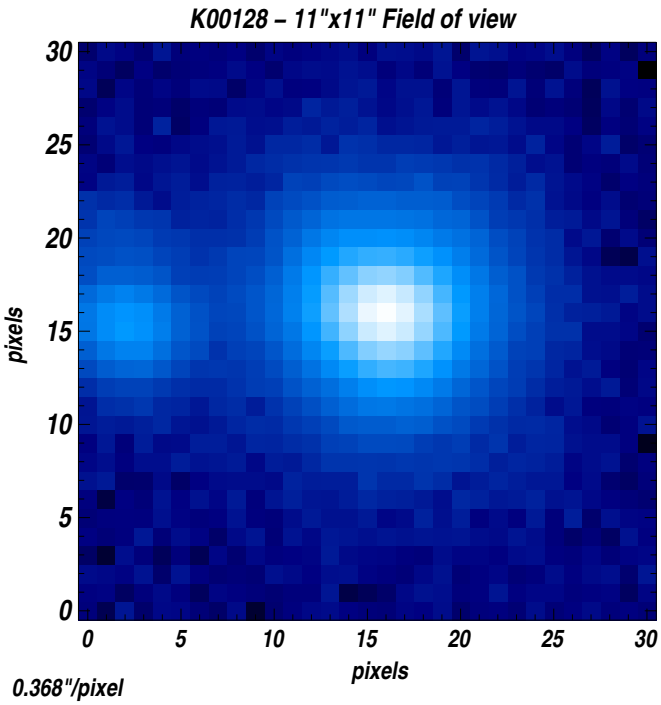

Figure 5. *I*-band image of the field centered on Kepler-15 (KOI-128) taken with the 1 m telescope at Lick Observatory. The scale is 11 × 11 arcsec, north is up and east is left. KIC 11359883—the other KIC star is the Kepler-15 aperture—is visible 4 arcsec to the east.

(A color version of this figure is available in the online journal.)

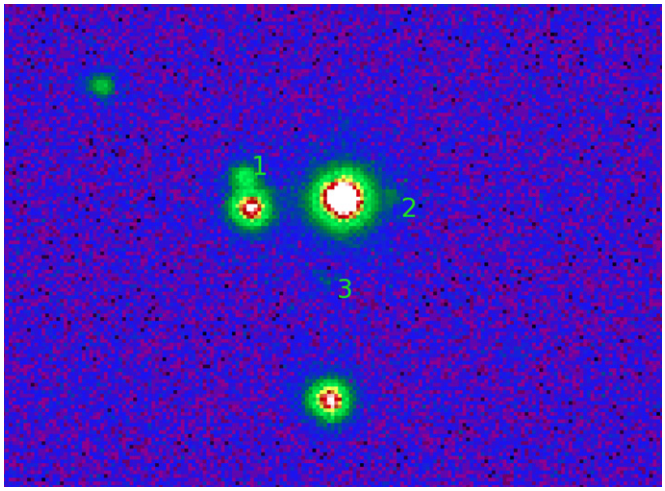

Figure 6. *J*-band image of the field around Kepler-15 (center) taken with UKIRT. North is up and east is left. The scale is ∼25 × 40 arcsec. We detect three additional objects located within the optimal aperture of Kepler-15 (besides KIC 11359883). Objects 1 and 2 are real, but object 3 is an artifact. The two other stars seen in this image to the far east and south are located outside the optimal aperture.

(A color version of this figure is available in the online journal.)

$K_p = 19.4 \pm 0.6$. Object 2 is very close to Kepler-15 and we estimate $K_p = 21.4 \pm 0.9$. Object 3 is an artifact caused by electronic cross-talk. We estimate the K_p values from the measured *J*-band magnitudes and the typical $K_p - J$ color according to the Besancon synthetic Galactic population model (Robin et al. 2003) for stars of this *J* magnitude at this place on the sky. Object 1 is also barely visible in the wings of the point-spread function of KIC 11359883 in the Lick *I*-band image.

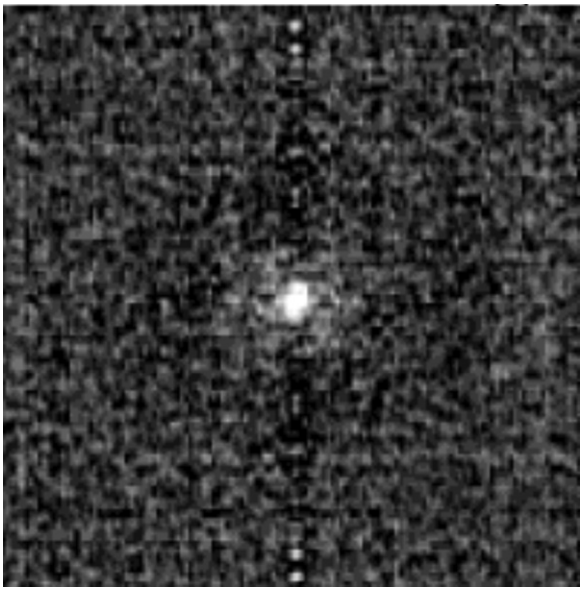

Figure 7. Reconstructed *R*-band speckle image of Kepler-15 taken with the WIYN telescope at Kitt Peak. No additional stars are detected within the annulus from 0.″05 to 1.″8 to a limit of (5σ) 3.52 mag fainter than the target star. The image is 2.″8 × 2.″8 and north is up and east is to the left.

We have also obtained speckle observations at the WIYN 3.5 m telescope located on Kitt Peak. The observations make use of the Differential Speckle Survey Instrument (DSSI), a recently upgraded speckle camera described in Horch et al. (2010) and Howell et al. (2011). The DSSI provides simultaneous observations in two filters by employing a dichroic beam splitter and two identical EMCCDs as the imagers. We observed Kepler-15 simultaneously in "V" and "R" bandpasses where "V" has a central wavelength of 5620 Å, and "R" has a central wavelength of 6920 Å, and each filter has an FWHM = 400 Å. The details of how we obtain, reduce, and analyze the speckle results and specifics about how they are used to eliminate false positives and aid in transit detection are described in Howell et al. (2011).

The speckle observations of the Kepler-15 were obtained on 2010 October 24 (UT) and consisted of five sets of 1000, 40 ms individual speckle images. Our *R*-band reconstructed image is shown in Figure 7 with details of the image composition described in Howell et al. (2011). Along with a nearly identical *V*-band reconstructed image, the speckle results reveal no companion star near Kepler-15 within the annulus from 0.″05 to 1.″8 to a limit of (5σ) 3.52 mag fainter in *R* and 3.16 mag fainter in *V* relative to the $K_p = 13.76$ target star.

As a result of the direct imaging of the field around Kepler-15 we found that two additional stars (besides KIC 11359883) are located within the optimal aperture of Kepler-15. However, both stars are fainter than $K_p = 19$ and have a negligible effect on the photometry. Only KIC 11359883 ($K_p = 15.99$) has a significant effect and we take the diluting effect of its light contribution into account for the light curve modeling.

3.3. Precise Radial Velocity Measurements

We performed precise RV follow-up observations of Kepler-15 with the HET (Ramsey et al. 1998) and its HRS spectrograph (Tull 1998). The queue-scheduled observing mode of the HET usually leads to the situation that on a given night data for many different projects and with different instruments are obtained. The observations are ranked according to priorities distributed by the HET time-allocation committees as well

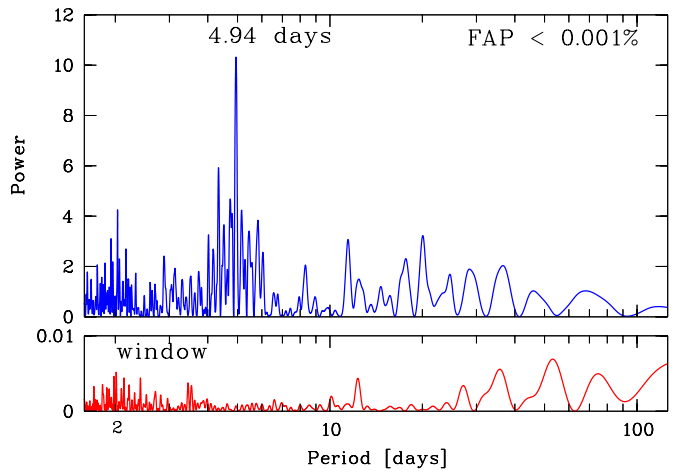

Figure 8. Lomb–Scargle periodogram of the HET/HRS RV results for Kepler-15. The top panel shows the power spectrum of the periodogram with a highly significant peak (false alarm probability FAP $< 10^{-5}$) at the transit period of 4.94 days. The lower panel displays the window function of the HET observations.

(A color version of this figure is available in the online journal.)

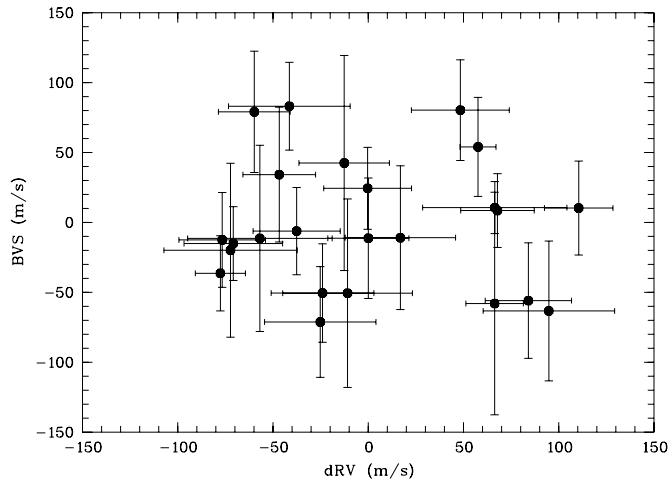

Figure 9. Correlation between the bisector velocity span (BVS) and the RV measurements of the 24 HET spectra. No correlation is detected (linear correlation coefficient is −0.076).

Table 2
Radial Velocity Measurements for Kepler-15

BJD (days)	dRV (m s^{-1})	err (m s^{-1})	Telescope
2455284.9813	57.6	9.5	HET
2455286.9710	−46.7	19.1	HET
2455335.8584	−59.8	18.8	HET
2455337.8690	−0.3	23.1	HET
2455346.8415	−56.9	38.0	HET
2455349.8134	16.9	29.0	HET
2455357.7918	48.4	25.7	HET
2455359.7847	0.1	21.3	HET
2455363.7848	67.8	19.3	HET
2455370.7339	−77.6	13.1	HET
2455395.6901	−76.7	22.7	HET
2455397.8812	94.8	34.5	HET
2455399.8848	−25.2	29.2	HET
2455405.6752	−72.3	35.0	HET
2455470.6934	−24.0	27.0	HET
2455494.6203	−70.9	25.9	HET
2455497.6337	66.4	15.1	HET
2455498.6031	−12.6	23.8	HET
2455501.6037	110.5	18.0	HET
2455502.5925	66.4	37.9	HET
2455504.5953	−37.6	22.9	HET
2455506.5891	84.1	22.7	HET
2455508.6009	−10.9	34.0	HET
2455509.5755	−41.4	31.9	HET
2455378.6493	148.5	19.0	NOT
2455384.7006	58.0	20.1	NOT
2455423.4036	136.4	26.2	NOT
2455425.4572	0.0	19.0	NOT
2455427.4408	130.9	20.8	NOT
2455432.4702	130.7	24.5	NOT

as additional timing constraints. We entered Kepler-15 into the HET queue to be observed in a quasi-random fashion with a cadence of a few days to allow proper sampling of the suspected 4.9 day RV orbit. We observed this target from 2010 March 29 until 2010 November 9. We collected 24 HRS spectra with the I_2-cell in the light path for precise RV measurements. Furthermore, we obtained one spectrum without the I_2-cell to serve as a stellar "template" for the RV computation and to better characterize the properties of the host star.

Because of the faintness of this star, the HRS setup we employed for the RV observations is slightly different from our standard planet search RV reduction pipeline (described in detail in Cochran et al. 2004). We used the 2 arcsec fiber to feed the light into the HRS. The cross-disperser setting was "600g5822," which corresponds to a wavelength coverage from 4814 to 6793 Å, thus covering the entire I_2 spectral range of 5000–6400 Å. We also used a wider slit to gain a higher throughput for this faint target, reducing the spectral resolving power to $R = \lambda/\Delta\lambda = 30{,}000$ (instead of our nominal $R = 60{,}000$). Moreover, two sky fibers allow us to simultaneously record the sky background and to properly subtract it from our data. The CCD was binned 2×2, which yields 4 pixels per resolution element. This new setup is better suited for observations of the faint *Kepler* targets. The exposure time for each observation was 1200 s. The mean S/N of the 24 spectra is 42 ± 6 per resolution element. As higher spectral resolution is advantageous for the template spectrum, we obtained this spectrum with $R = 60{,}000$ and a longer exposure time of 2700 s. We computed precise differential RVs with our *Austral* I_2-cell data modeling algorithm (Endl et al. 2000). The HET/HRS RV data are listed in Table 2. The data have an overall rms-scatter of 60 m s^{-1} and average internal errors of 25 ± 8 m s^{-1}.

We performed a period search in our HET RV data set using the classic Lomb–Scargle periodogram (Lomb 1976; Scargle 1982). Figure 8 displays the power spectrum over the period range from 2 to 100 days. The highest peak is located at a period of 4.94 days. This is an independent confirmation of the transit period. The signal is also statistically highly significant, we estimate a false alarm probability (FAP) of less than 10^{-5} using a bootstrap randomization scheme (Kürster et al. 1997).

We have also determined line bisectors from the HET spectra. As we could use only the small fraction of the available spectral range that lies outside the I_2 region (5000–6400 Å) the uncertainties in the bisector velocity span (BVS) are quite large, the average error of the BVS measurements is 43 ± 17 m s^{-1}, and they have a total rms-scatter of 46 m s^{-1}. The bisector measurements are given in Table 3. Figure 9 shows

Table 3
Bisector Measurements for Kepler-15

BJD (days)	Bisector (m s^{-1})	bserr (m s^{-1})	Spectrograph
2455284.9813	54.0	35.4	HRS
2455286.9710	34.2	48.2	HRS
2455335.8584	79.1	43.4	HRS
2455337.8690	24.4	29.3	HRS
2455346.8415	−11.4	66.6	HRS
2455349.8134	−10.9	51.4	HRS
2455357.7918	80.3	36.0	HRS
2455359.7847	−11.3	43.1	HRS
2455363.7848	8.5	26.4	HRS
2455370.7339	−36.4	26.9	HRS
2455395.6901	−12.5	33.9	HRS
2455397.8812	−63.3	50.0	HRS
2455399.8848	−71.2	39.6	HRS
2455405.6752	−19.9	62.2	HRS
2455470.6934	−50.5	35.2	HRS
2455494.6203	−15.1	26.4	HRS
2455497.6337	−58.0	79.6	HRS
2455498.6030	42.5	76.9	HRS
2455501.6037	10.3	33.6	HRS
2455502.5925	10.6	18.6	HRS
2455504.5953	−6.2	31.2	HRS
2455506.5891	−55.9	41.3	HRS
2455508.6009	−50.6	67.4	HRS
2455509.5755	83.1	31.4	HRS
2455378.6493	−14.2	12.6	FIES
2455384.7006	−10.6	15.7	FIES
2455423.4036	1.6	13.4	FIES
2455425.4572	−1.9	10.1	FIES
2455427.4408	3.9	14.4	FIES
2455432.4702	21.2	16.4	FIES

the correlation plot of BVS values versus RV measurements. The linear correlation coefficient −0.076 corresponds to a 72% probability that the null-hypothesis of zero correlation is true. This further strengthens the case that the RV modulation is due to an orbiting companion.

We have also taken six spectra between 2010 July and August using the FIES at the 2.5 m NOT at La Palma, Spain (Djupvik & Andersen 2010). We used the medium- and the high-resolution fibers (1″.3 projected diameter) with resolving powers of $R \approx 46{,}000$ and 67,000, respectively, giving a wavelength coverage of ∼3600–7400 Å. We used the wavelength range from approximately ∼4100–5600 Å to determine the RVs following the procedures described in Buchhave et al. (2010). The exposure time was between 2400 and 3600 s, yielding an S/N from 22 to 30 pixel^{-1} in the wavelength range used. The FIES RV results are also given in Table 2. Like in the case of the reconnaissance spectra, we checked the Ca II H & K line emission levels and did not find any sign of strong chromospheric emission.

We also determined the line bisectors for the six FIES spectra. They have a higher precision than the HRS results since we could use the entire spectrum for the analysis (FIES does not use an I_2-cell). The FIES bisector data are listed in Table 3 and shown as a function of orbital phase in Figure 10. The average uncertainty of the FIES bisector measurements is 13.8 ± 2.3 m s^{-1} and their total scatter is 12.5 m s^{-1}. They appear to be constant within the measurement uncertainties. The linear correlation coefficient is 0.31 corresponding to a 55% probability for the null-hypothesis of zero correlation.

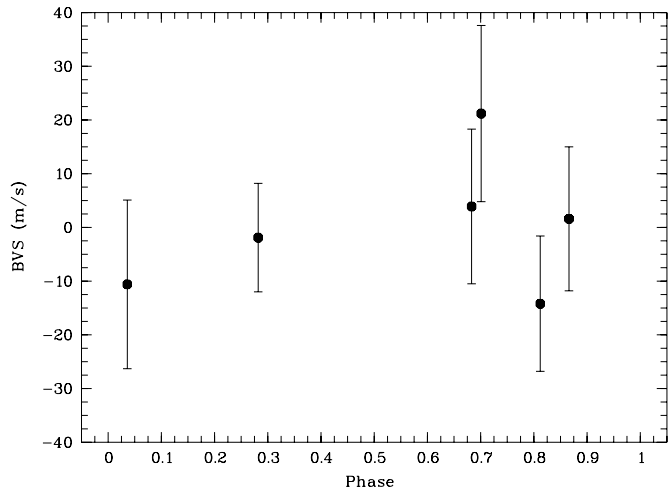

Figure 10. FIES line bisectors and their uncertainties as a function of transit/orbital phase of Kepler-15. We detect no significant variability.

4. RESULTS

4.1. Host Star Characterization

We determined stellar parameters using the local thermodynamic equilibrium (LTE) line analysis and spectral synthesis code MOOG[20] (Sneden 1973), together with a grid of Kurucz (1993) ATLAS9 model atmospheres. The method used is virtually identical to that described in Brugamyer et al. (2011). To check this method, we first measured the equivalent widths of a carefully selected list of 48 neutral iron lines and 11 singly ionized iron lines in a spectrum of the daytime sky, taken using the same instrumental setup and configuration as that used for Kepler-15. MOOG force fits abundances to match these measured equivalent widths, using declared atomic line parameters. By assuming excitation equilibrium, we constrained the stellar temperature by eliminating any trends with excitation potential; assuming ionization equilibrium, we constrained the stellar surface gravity by forcing the derived iron abundance using neutral lines to match that of singly ionized lines. The microturbulent velocity was constrained by eliminating any trend with reduced equivalent width (=EW/λ). Our derived stellar parameters for the Sun (using our daytime sky spectrum) are as follows: $T_{\rm eff} = 5755 \pm 70$ K, $\log g = 4.48 \pm 0.09$ dex, Vmic $= 1.07 \pm 0.06$ km s^{-1}, and $\log \epsilon$ (Fe) $= 7.53 \pm 0.05$ dex, demonstrating the accuracy of our technique.

The process described above was repeated for the HET/HRS spectrum taken without the I_2-cell of Kepler-15. We took the difference, on a line-by-line basis, of the derived iron abundance from each line. Our quoted iron abundance is therefore differential with respect to the Sun. To estimate the rotational velocity of the star, we synthesized three 5 Å wide spectral regions in the range 5640–5690 Å and adjusted the Gaussian and rotational broadening parameters until the best fit (by eye) was found to the observed spectrum. The results of our analysis yield the following stellar parameters for Kepler-15: $T_{\rm eff} = 5595 \pm 120$ K, $\log g = 4.23 \pm 0.2$, Vmic $= 1.09 \pm 0.1$ km s^{-1}, [Fe/H] $= +0.36 \pm 0.07$, and $v \sin i = 2 \pm 2$ km s^{-1}. The preliminary results from the reconnaissance spectroscopy ($T_{\rm eff} \approx 5500$ K, $\log g = 4.0$ and 4.5, and $v \sin i = 2$ km s^{-1}) compare very well with this improved spectroscopic analysis.

[20] Available at http://www.as.utexas.edu/~chris/moog.html

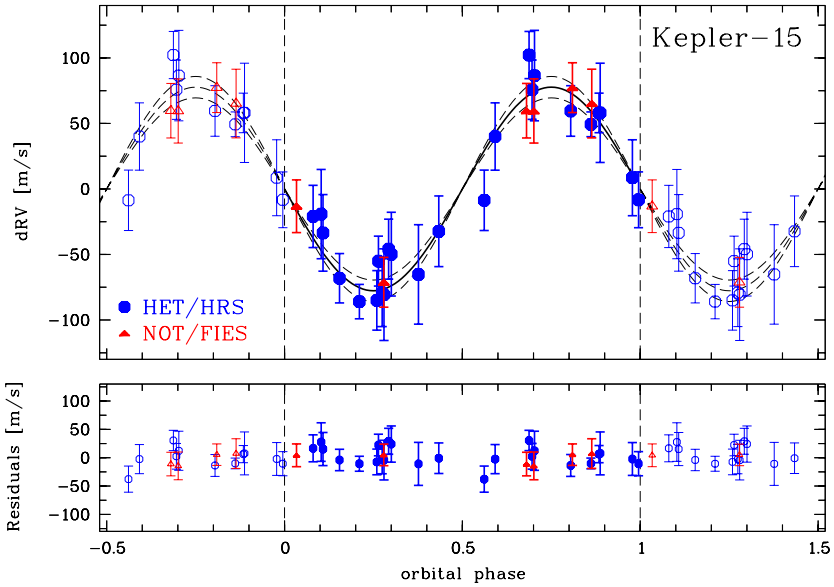

Figure 11. HET/HRS (circles) and NOT/FIES (triangles) RV data and the best-fit orbital solution (solid line) phased to the transit period of 4.94 days (top panel). The orbit with a semi-amplitude K of 78.7 ± 9.1 m s^{-1} is shown as a solid line and the dashed lines represent the 1σ uncertainty in K. The amplitude of the orbit corresponds to a mass of 0.66 ± 0.08 $M_{\rm Jup}$ for the planetary companion. The bottom panel shows the residuals: the 24 HRS points have a residual rms scatter of 16.9 m s^{-1} and the 6 FIES points have a residual rms scatter of 9.6 m s^{-1}. (The data are repeated for a second cycle.)

(A color version of this figure is available in the online journal.)

4.2. Orbital Solution and Planet Parameters

We first used Gaussfit (Jefferys et al. 1988) to fit a Keplerian orbit to our RV data alone. The best-fit value for a circular orbit fit are $P = 4.939 \pm 0.0034$ days, RV semi-amplitude $K = 74.9 \pm 3.3$ m s^{-1}, and time of periastron $T_0 = 54974.03 \pm 0.28$ JD. The orbital phase we find from fitting the RV data alone is slightly offset to the transit phase by 0.24 days, but this is within the 1σ uncertainty of T_0. The reduced χ^2 of this fit is 0.55, indicating that a circular orbit model is more than adequate to describe the RV data. Nevertheless, we also performed a fit including the orbital eccentricity as a free parameter. We found $e = 0.06 \pm 0.06$, consistent with zero. When we also include a linear slope we find a best-fit slope of $+0.12 \pm 0.04$ m s^{-1} day^{-1}. $\chi^2_{\rm red}$ of the orbit+slope model is 0.39. This slope could indicate the presence of an outer companion with a period exceeding our time baseline. However, as the $\chi^2_{\rm red}$ is already below 1, the confirmation of this slope needs to await future observations. Including the slope in the model has virtually no effect on the RV-amplitude ($K = 74.9 \pm 3.3$ m s^{-1} without the slope and $K = 74.6 \pm 3.0$ m s^{-1} with the slope) and hence the mass of the companion.

We then used a Markov Chain Monte Carlo (MCMC) algorithm to perform a simultaneous fit to the light curve and the RV results. This analysis was performed using the 24 HET RV measurements and the Q1 through Q6 *Kepler* photometry. The model fits for $\rho_\star$, T_0, Period, b, $r/R_\star$, $e \sin\omega$, $e \cos\omega$, γ, and the photometric zero point. The transit shape is characterized by the Mandel–Agol analytic derivations (Mandel & Agol 2002) and the planetary orbit is assumed to be Keplerian. We use nonlinear limb-darkening parameters derived by A. Prsa (2011, private communication). The best-fit model is computed by simultaneously fitting RV measurements and Kepler photometry and then minimizing the chi-square statistic with a Levenberg–Marquart method. To obtain probability distributions, the best-fit model is used to seed an MCMC computation. Our MCMC algorithm employs a hybrid sampler based on Gregory (2011) that uses a Gibb sampler or a buffer of previously computed chain points to generate proposals to jump to new locations in parameter space. The addition of the buffer allows for a calculation of vectorized jumps that allow for efficient sampling of highly correlated parameter space. Specifically, we employed a correlated parameter sampler as discussed in Section 3 of Gregory (2011). The MCMC distributions are shown in Figure 12.

The results of this MCMC modeling are summarized in Table 4. For all parameters we list the median values along with their 68% uncertainty interval ($\pm 1\sigma$) based on the MCMC distributions. The transit ephemeris is $T_0 = 69.328651^{+0.000084}_{-0.000096}$ (BJD−2454900) and the period is $P = 4.942782 \pm 0.0000013$ days. The transit has a depth of $11{,}127.7^{+12.8}_{-14.4}$ ppm. Taking into account the diluting effect of the other star in the aperture (97.0% ± 0.003% of the light in the aperture comes from Kepler-15) we find a radius ratio of $R_{\rm planet}/R_* = 0.09960^{+0.00055}_{-0.00053}$. The RV semi-amplitude K is $78.7^{+8.5}_{-9.1}$ m s^{-1}. The orbital eccentricity was allowed as a free parameter during the modeling process, but again we find no strong indication for an eccentric orbit ($e \sin\omega = -0.123^{+0.089}_{-0.110}$, $e \cos\omega = 0.053^{+0.086}_{-0.079}$). Figure 11 displays the HET/HRS and the NOT/FIES results compared to the RV orbit (assuming $e = 0$). The reduced χ^2 of this fit is 0.52, indicating that our RV error bars are slightly overestimated. The residual rms scatter for the two RV data set is 16.9 m s^{-1} for the HET/HRS data and 9.6 m s^{-1} for the NOT/FIES data.

The distribution of $\rho_\star$ from the model fit above and $T_{\rm eff}$ and [Fe/H] from the spectroscopic determination are used together to match Yonsei–Yale (Y^2) models (Yi et al. 2001). This is known as the "$\rho_\star$ method" (see, e.g., Sozetti et al. 2007; Brown 2010). The probability distributions of the matching stellar parameters, $M_\star$, $R_\star$, age, luminosity are also shown in Figure 12. From isochrone fitting we derive a mass for the star of $1.018^{+0.044}_{-0.052}$ $M_\odot$, a radius of $0.992^{+0.058}_{-0.070}$ $R_\odot$, and an age of $3.7^{+3.5}_{-1.6}$ Gyr. The log g from the isochrone fit is $4.46^{+0.053}_{-0.050}$, 0.2 dex higher than the spectroscopically derived log g value of 4.23 ± 0.2. A systematic difference in log g values for high metallicity stars has been discussed previously for Kepler-6 (Dunham et al.

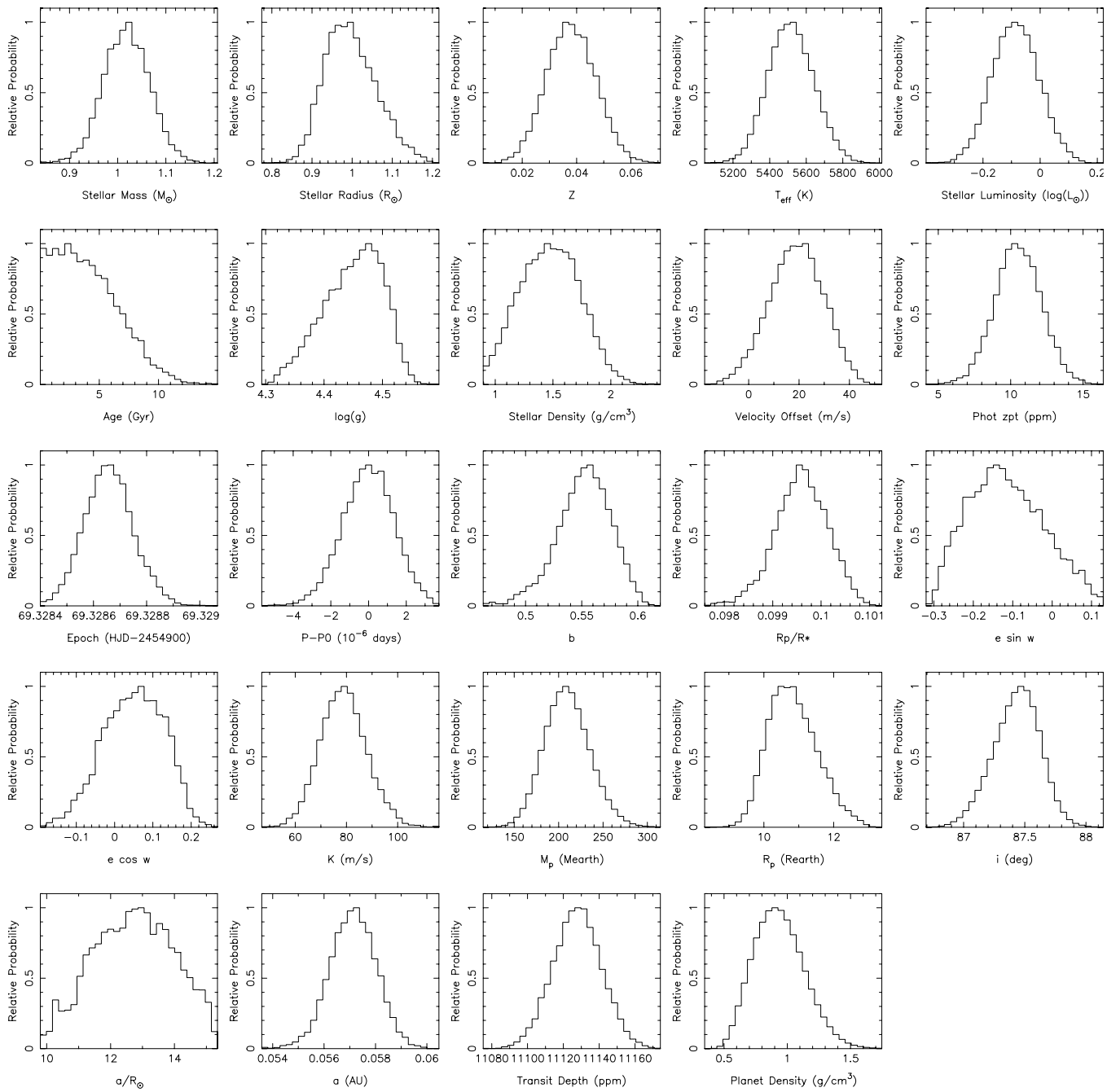

Figure 12. Markov Chain Monte Carlo distributions for the model parameters for the Kepler-15 system. The resulting values and uncertainties of the system parameters are listed in Table 4. For the period value we plot the difference to $P_0 = 4.942782$ days.

2010). We note that the difference in our case is the opposite (the spectroscopic log g is lower, for Kepler-6 it was higher by 0.35 dex). However, the error bars of both methods still overlap for Kepler-15. All stellar parameters from the isochrone fit are also listed in Table 4.

The planetary orbit and parameters are derived by using the Markov Chains from the model and isochrone fits. Random chains are selected from each fit to calculate the planet mass, radius, semimajor axis, $a/R_\star$, and presented in Figure 12 and Table 4.

5. DISCUSSION

After passing all tests and observational diagnostics, from photometric centroid shifts to spectroscopic line bisectors, and the fact that an RV orbit in period and phase with the transit ephemeris is detected, we conclude that Kepler-15b is indeed a new transiting planet.

All our currently available data suggest a planet with a mass of $0.66^{+0.08}_{-0.09}\,M_{\rm Jup}$, a radius of $0.96^{+0.06}_{-0.07}\,R_{\rm Jup}$, and a mean density of 0.9 ± 0.2 g cm^{-3} orbiting a metal-rich ([Fe/H] $= 0.36 \pm 0.07$) G-type star every 4.94 days. Kepler-15 is tied with Kepler-6 as the most metal-rich host star of all currently published *Kepler* planets.

Initially, we suspected a large planetary radius for Kepler-15b as the KIC value for the stellar radius is $1.4\,R_\odot$, which would translate to a companion radius of $\approx 1.5\,R_{\rm Jup}$. This large planetary radius prompted our ground-based follow-up campaign to confirm and characterize this system. Interestingly,

Table 4
Parameters of the Kepler-15 Transiting System

Parameter (unit)	Value	$+1\sigma$	-1σ	Notes
Period (days)	4.942782	+0.0000013	−0.0000013	
T_0 (BJD)	2454969.328651	+0.000084	−0.000096	
$\rho_\star$ (g cm^{-3})	1.47	+0.26	−0.28	
b	0.554	+0.023	−0.024	
$R_{\rm planet}/R_\star$	0.0996	+0.00055	−0.00053	
i (deg)	87.44	+0.18	−0.20	
$a/R_\star$	12.8	+1.2	−1.5	
$M_\star$ [$M_\odot$]	1.018	+0.044	−0.052	(isochrone fit)
$R_\star$ [$R_\odot$]	0.992	+0.058	−0.070	(isochrone fit)
Age (Gyr)	3.7	+1.5	−3.6	(isochrone fit)
$T_{\rm eff}$ (K)	5515	+122	−130	(isochrone fit)
log $L/L_\odot$	−0.087	+0.078	−0.088	(isochrone fit)
log g (cgs)	4.46	+0.053	−0.050	(isochrone fit)
log g (cgs)	4.23	+0.2	−0.2	(spectroscopic fit)
[Fe/H]	0.36	+0.07	−0.07	(spectroscopic fit)
$V_{\rm rot}$ (km s^{-1})	2.0	+2.0	−2.0	(spectroscopic fit)
RV (km s^{-1})	−20.0	+1.0	−1.0	(spectroscopic fit)
$R_{\rm planet}$ ($R_{\rm Jup}$)	0.96	+0.06	−0.07	
K (m s^{-1})	78.7	+8.5	−9.5	
$e \sin\omega$	−0.123	+0.089	−0.110	
$e \cos\omega$	0.053	+0.086	−0.079	
$M_{\rm planet}$ ($M_{\rm Jup}$)	0.66	+0.08	−0.09	
a (AU)	0.05714	+0.00086	−0.00093	
$\rho_{\rm planet}$ (g cm^{-3})	0.93	+0.18	−0.22	

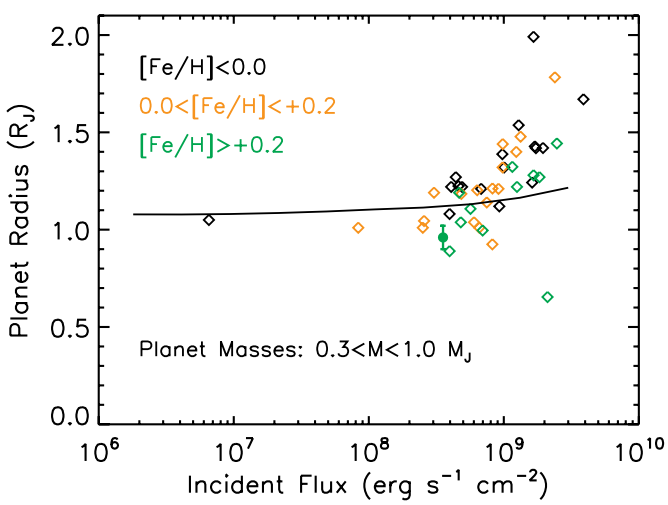

Figure 13. Planet mass vs. radius for a collection of transiting planets with masses from 0.3 to 1.0 $M_{\rm Jup}$. Values are taken from http://www.inscience.ch/transits/. Kepler-15 is shown as a filled circle. The solid curve is for a 1 $M_{\rm Jup}$ model planet at 4.5 Gyr (Miller et al. 2009). While many planets are inflated relative to this curve, Kepler-15 is clearly below it. While a radius-inflation mechanism could still be at work in this planet, the small radius indicates that the planet is rich in heavy elements.

(A color version of this figure is available in the online journal.)

our results demonstrate rather the opposite. Figure 13 shows that the planet's radius is modestly smaller than planets of similar mass and irradiation level. This suggests that the planet is more enriched in heavy elements than most other transiting planets. Given the high stellar metallicity, and the connection between stellar metallicity and planetary heavy elements (Guillot et al. 2006; Burrows et al. 2007; Miller & Fortney 2011), this is is not surprising.

Figure 13 shows planetary radii using three different stellar metallicity bins, from [Fe/H] $<$ 0.0, 0.0 $\leqslant$ [Fe/H] $<$ 0.2, [Fe/H] $\geqslant$ 0.2. Compared to a solar composition planetary model from Fortney et al. (2007), the planets orbiting metal-poor parent stars (black diamonds) are preferentially above the curve, while those around metal-rich parent stars (green diamonds) are preferentially below the curve. This suggests that while a radius inflation mechanism is a general feature of all close-in giant planets, the radius increase is diminished or canceled out in metal-rich systems. Laughlin et al. (2011) have found a strong correlation between metal-rich parent stars and smaller planetary radii, for a collection of 90 transiting planets, as can also been seen from the three metallicity bins in Figure 12.

We use the tables of Fortney et al. (2007) to estimate a heavy element mass of Kepler-15b of at least 30–40 Earth masses. Given the uncertain nature of the radius inflation mechanism, this estimate should be considered a lower limit. Recently, Miller & Fortney (2011) have investigated the structure of cooler ($T_{\rm eff}$ $<$ 1000 K) transiting exoplanets, where the radius inflation mechanism does not appear to be operating. This allows for giant planet heavy element enrichments to be determined with some confidence. They find that 40–100 Earth masses of heavy elements are a common feature of all extrasolar gas giants around parent stars with [Fe/H] $>$ 0.3.

Kepler-15b is the first giant planet from the *Kepler* mission that we confirmed with the HET, demonstrating the capability of this facility as an integral part of the ground-based spectroscopic follow-up effort of the *Kepler* mission. The HET will obtain a major upgrade to its secondary tracker assembly to allow a wider field of view. This upgrade will start in fall 2011. During the telescope downtime the HRS will also undergo a major upgrade, including more efficient optics and fibers, as well as image slicers, to boost the overall throughput by several factors. Once the HET is back on sky in early 2012, these improvements should allow us to use the HET/HRS also for the confirmation and validation of low mass *Kepler* planet candidates in the

Neptune and Super-Earth range, similar to Kepler-10b (Batalha et al. 2011).

Funding for this Discovery mission is provided by NASA's Science Mission Directorate. We thank the hundreds of people who make this mission successful. The Hobby–Eberly Telescope (HET) is a joint project of the University of Texas at Austin, the Pennsylvania State University, Stanford University, Ludwig-Maximilians-Universität München, and Georg-August-Universität Göttingen. The HET is named in honor of its principal benefactors, William P. Hobby and Robert E. Eberly. Based in part on observations made with the Nordic Optical Telescope, operated on the island of La Palma jointly by Denmark, Finland, Iceland, Norway, and Sweden, in the Spanish Observatorio del Roque de los Muchachos of the Instituto de Astrofisica de Canarias. We also thank the anonymous referee for many helpful suggestions to improve the manuscript.

REFERENCES

Batalha, N., Borucki, W., Bryson, S., et al. 2011, ApJ, 729, 27
Borucki, W. J., Koch, D., Basri, G., et al. 2010, Science, 327, 977
Borucki, W. J., Koch, D. J., Basri, G., et al. 2011, ApJ, 736, 19
Brown, T. M. 2010, ApJ, 709, 535
Brown, T. M., Latham, D. W., Everett, M. E., & Esquerdo, G. A. 2011, AJ, 142, 112
Brugamyer, E., Dodson-Robinson, S. E., Cochran, W. D., & Sneden, C. 2011, ApJ, 738, 97
Bryson, S. T., Tenenbaum, P., Jenkins, J. M., et al. 2010, ApJ, 713, L97
Buchhave, L. A., Bakos, G. A., Hartman, J. D., et al. 2010, ApJ, 720, 1118
Burrows, A., Hubeny, I., Budaj, J., & Hubbard, W. B. 2007, ApJ, 661, 502
Cochran, W. D., Endl, M., McArthur, B., et al. 2004, ApJ, 611, 133
Cutri, R. M., Skrutskie, M. F., van Dyk, S., et al. 2003, VizieR On-line Data Catalog: II/246
Djupvik, A. A., & Andersen, J. 2010, in Highlights of Spanish Astrophysics V, ed. J. M. Diego, L. J. Goicoechea, J. I. González-Serrano, & J. Gorgas (Berlin: Springer), 211
Désert, J.-M., Charbonneau, D., Demory, B.-O., et al. 2011, ApJS, 197, 14
Dunham, E. W., Borucki, W. J., Koch, D. G., et al. 2010, ApJ, 713, L136
Endl, M., Kürster, M., & Els, S. 2000, A&A, 362, 585
Fortney, J. J., Marley, M. S., & Barnes, J. W. 2007, ApJ, 659, 1661
Gautier, T. N., Batalha, N. M., Borucki, W. J., et al. 2010, arXiv:1001.0352
Gregory, P. C. 2011, MNRAS, 410, 94
Guillot, T., Santos, N. C., Pont, F., et al. 2006, A&A, 453, L21
Horch, E. P., Gomez, S. C., Sherry, W. H., et al. 2010, AJ, 141, 45
Howell, S. B., Everett, M. E., Sherry, W., Horch, E., & Ciardi, D. R. 2011, AJ, 142, 19
Jefferys, W. H., Fitzpatrick, M. J., & McArthur, B. E. 1988, Celest. Mech., 41, 39
Jenkins, J. M., Borucki, W. J., Koch, D. G., et al. 2010a, ApJ, 724, 1108
Jenkins, J. M., Caldwell, D. A., Chandrasekaran, H., et al. 2010b, ApJ, 713, L87
Koch, D. G., Borucki, W. J., Basri, G., et al. 2010, ApJ, 713, L79
Kürster, M., Schmitt, J. H. M. M., Cutispoto, G., & Dennerl, K. 1997, A&A, 320, 831
Kurucz, R. 1993, ATLAS9 Stellar Atmosphere Programs and 2 km/s Grid (Kurucz CD-ROM No. 13.; Cambridge: Smithsonian Astrophys. Obs.)
Latham, D. W., Borucki, W. J., Koch, D. G., et al. 2010, ApJ, 713, L140
Laughlin, G., Crismani, M., & Adams, F. C. 2011, ApJ, 729, 7
Lomb, N. R. 1976, Ap&SS, 39, 447
Mandel, K., & Agol, E. 2002, ApJ, 580, L171
Miller, N., & Fortney, J. J. 2011, ApJ, 736, 29
Miller, N., Fortney, J. J., & Jackson, B. 2009, ApJ, 702, 1413
Ramsey, L. W., Adams, M. T., Barnes, Thomas G., et al. 1998, Proc. SPIE, 3352, 34
Robin, A. C., Reylé, C., Derriére, S., & Picaud, S. 2003, A&A, 409, 523
Santerne, A., Diaz, R. F., Bouchy, F., et al. 2011, A&A, 528, 63
Scargle, J. D. 1982, ApJ, 263, 835
Sneden, C. A. 1973, PhD thesis, Univ. Texas at Austin
Sozetti, A., Torres, G., Charbonneau, D., et al. 2007, ApJ, 664, 1190
Torres, G., Fressin, F., Batalha, N. M., et al. 2011, ApJ, 727, 24
Tull, R. G. 1998, Proc. SPIE, 3355, 387
Tull, R. G., MacQueen, P. J., Sneden, C., & Lambert, D. L. 1995, PASP, 107, 251
Yi, S., Demarque, P., Kim, Y.-C., et al. 2001, ApJS, 136, 417